The ISME Journal
https://doi.org/10.1038/s41396-018-0188-8

BRIEF COMMUNICATION

Observed metabolic asymmetry within soybean root nodules reflects unexpected complexity in rhizobacteria-legume metabolite exchange

Dušan Veličković[1] · Beverly J. Agtuca[2] · Sylwia A. Stopka[3] · Akos Vertes[3] · David W. Koppenaal[1] · Ljiljana Paša-Tolić[1] · Gary Stacey[2] · Christopher R. Anderton[1]

Received: 22 November 2017 / Revised: 2 February 2018 / Accepted: 26 February 2018

Abstract

In this study, the three-dimensional spatial distributions of a number of metabolites involved in regulating symbiosis and biological nitrogen fixation (BNF) within soybean root nodules were revealed using matrix-assisted laser desorption/ionization mass spectrometry imaging (MALDI-MSI). While many metabolites exhibited distinct spatial compartmentalization, some metabolites were asymmetrically distributed throughout the nodule (e.g., S-adenosylmethionine). These results establish a more complex metabolic view of plant–bacteria symbiosis (and BNF) within soybean nodules than previously hypothesized. Collectively these findings suggest that spatial perspectives in metabolic regulation should be considered to unravel the overall complexity of interacting organisms, like those relating to associations of nitrogen-fixing bacteria with host plants.

The symbiotic association between nitrogen-fixing soil bacteria (Rhizobiaceae) and plants of the family Leguminosae generate specialized organs called root nodules [1]. Elucidating metabolic processes within these plant organs, where biological nitrogen fixation (BNF) occurs, is essential for developing more sustainable agricultural practices, for example. Generally, there are two classes of nodules: (i) indeterminate nodules, such as those formed on alfalfa or pea, and (ii) determinate nodules, such as those formed on soybean or Lotus. Indeterminate nodules retain a terminal, apical meristem, and have been extensively studied, including by MALDI-MSI [2, 3]. This is in part because the full ontogeny of nodule development—from apical infection, bacteroid differentiation, nitrogen fixation, and basal senescence—is preserved longitudinally [4]. In contrast, determinate nodules lack an apical meristem and develop in principle by cellular expansion after invading rhizobia induce initial plant cell division. The result is that the globular soybean nodule does not preserve the preceding infection events. Accordingly, this has led in large part to the simplified view that soybean nodules are basically uniform in their metabolism, albeit with the presence of microscopically distinct compartments—i.e., outer cortex, inner cortex, and infection zone [4]. Recently, our group profiled the metabolome of intact soybean root nodules along with its individual biological components using laser ablation electrospray ionization mass spectrometry [5]. This method, nevertheless, provided limited spatially resolved metabolic information on the anatomical compartments of the nodule. On the contrary, the high (spatial and mass)-resolution molecular tomography described in the present study revealed unexpected complexity in the soybean nodule metabolism.

Herein, we spatially resolved the distribution of an array of metabolites within soybean nodules, using matrix-assisted laser desorption/ionization Fourier transform ion cyclotron resonance mass spectrometry imaging (MALDI-FTICR-MSI) [6].

Electronic supplementary material The online version of this article (https://doi.org/10.1038/s41396-018-0188-8) contains supplementary material, which is available to authorized users.

✉ Christopher R. Anderton
Christopher.Anderton@pnnl.gov

[1] Environmental Molecular Sciences Laboratory, Earth and Biological Sciences Directorate, Pacific Northwest National Laboratory, 902 Battelle Boulevard, Richland, WA 99354, USA

[2] Divisions of Plant Sciences and Biochemistry, C. S. Bond Life Sciences Center, University of Missouri, Columbia, MO 65211, USA

[3] Department of Chemistry, The George Washington University, Washington, DC 20052, USA

Published online: 13 June 2018

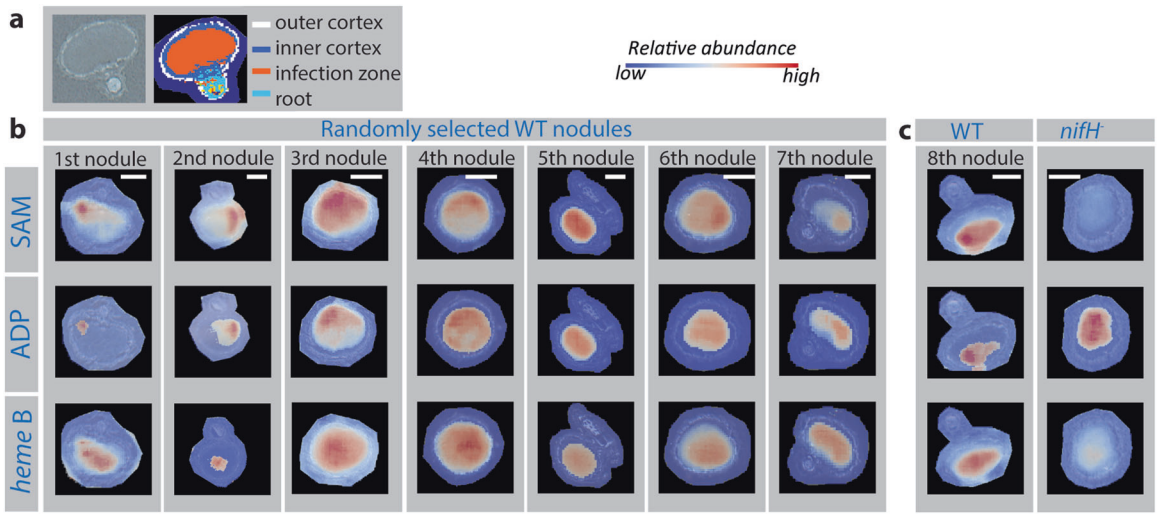

Fig. 1 **a** Anatomy of the soybean nodule as viewed through an optical image of a section (left) and the MALDI spectral spatial segmentation, which distinguishes areas based on their spectral composition (right). **b** Distribution of SAM, ADP, and *heme* B in the central cross-section of seven randomly selected WT nodules. Nodules were analyzed in different experiments to minimize analytical bias. In nodule No 5, SAM and *heme* B show symmetrical distribution pattern, which suggest that asymmetry in nodule metabolism can be consequence of nodule development over time. **c** For SAM, ADP, and *heme B* imaged in WT and *nif*H$^-$ nodules, both nodules were imaged in the same experiment, so that the relative intensity of ion signals can be compared. Scale bars are 1 mm

The value of this methodology is illustrated in Supporting Fig. 1. Among the approximately 140 annotated metabolites, most were co-localized within distinct anatomical compartments (Supporting Figs. 2–3, Supporting Tables 1–3). However, a few of the metabolites, including S-adenosylmethionine (SAM) and ADP (Fig. 1), showed a pronounced asymmetric distribution throughout the central zone of the nodule. This finding contradicts the long-standing hypothesis about metabolic homogeneity of this region within the soybean nodule [4], and points to a previously unacknowledged biochemical complexity in symbiotic plant–microbe interactions. For example, *heme* B, an essential molecule for providing microaerobic conditions during BNF [7], maintains a symmetric distribution within the infection zone, radially decreasing in abundance (Fig. 1b, bottom). Whereas the asymmetric distribution of SAM throughout the infection zone sheds a different light in its role in downstream BNF processes, given that SAM occupies a central role in both polyamine [8] and phosphatidylcholine (PCs) biosynthesis [9], molecules involved in nodule growth [8] and rhizobia-plant recognition [9], respectively. Further, ADP plays a central role during BNF, and its abundance is a key indicator of the energetic and oxidative state within the nodule [10]. Interestingly, it seems that ADP and SAM share the same distribution pattern (Pearson correlation coefficient of 0.80, Supporting Table 4), which is perhaps a consequence of ADP's involvement in SAM biosynthesis [11]. We additionally tested the importance of SAM and ADP during BNF by imaging the relative abundance and distribution of these metabolites in nodules inoculated with mutant rhizobia that could not efficiently fix nitrogen (*nif*H$^-$) (Fig. 1c). As expected, *heme* B presence in *nif*H$^-$ nodules was decreased compared to wild-type (WT) strain, given that the observable reddish pigment indicative of leghemoglobin presence is significantly diminished in the *nif*H$^-$ infection zone in comparison to the infection zone of the WT strain (Supporting Fig. S4). Additionally, compared to WT, the *nif*H$^-$ mutant produces substantially less SAM, and the noticeable divergence in ADP content and distribution between *nif*H$^-$ and WT nodules confirms their different energetic requirements. Other metabolites that show noticeable divergence between WT and *nif*H$^-$ mutant soybean nodules can be found in Supporting Fig. S5.

Further exploration of metabolic distributions within soybean root nodules was performed by molecular tomography (Fig. 2e, f). Here, conventional two-dimensional (2D) MALDI-FTICR-MSI analyses of serial sections traversing through the entire soybean nodule were acquired and subsequently these images were reconstructed into a three-dimensional (3D) MALDI-FTICR-MS image (Fig. 2a) [12]. Tomographically, three distinct microscopic compartments were readily visualized by mapping characteristic metabolites (Fig. 2b). Further, tomography revealed that SAM asymmetry (Fig. 2c) was consistent throughout the organ, whereas *heme* B is symmetrically localized throughout the infection region (Fig. 2d).

To elucidate possible causes for the asymmetric distribution of SAM, molecules within the two main metabolic pathways where SAM is involved during BNF were examined (Fig. 2e, f). Here, the distribution of molecules involved in polyamine biosynthesis exhibit an approximately uniform

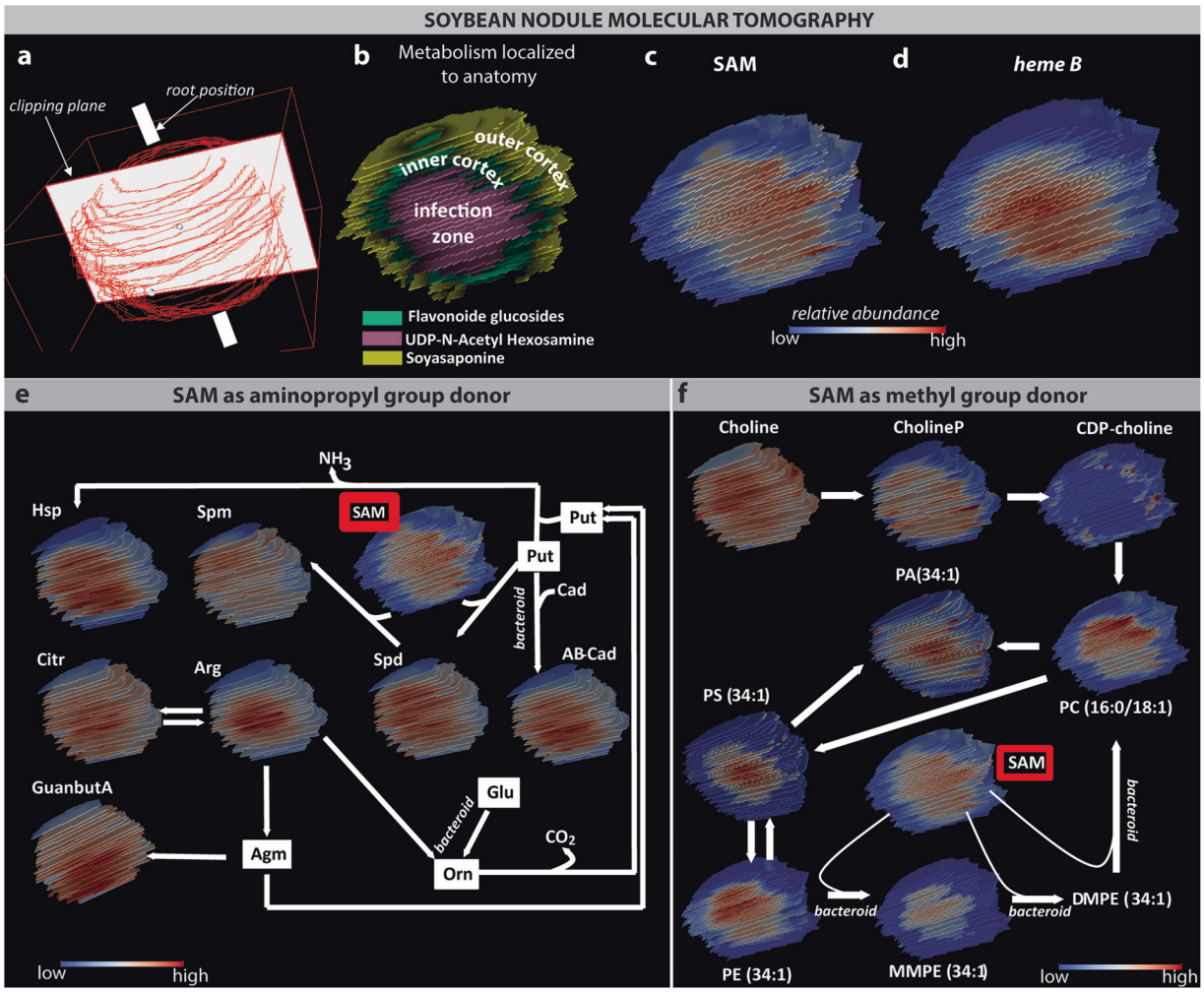

Fig. 2 3D-MALDI-FTICR-MSI of soybean root nodule metabolism. **a** Scheme illustrating the construction of the tomography image from 2D images. Resulting 3D localization of (**b**) three microscopic anatomical regions imaged by characteristic compounds, where UDP-N-acetyl hexosamine is co-localized with the infection zone, flavonoid glycoside is co-localized with the inner cortex, and soyasaponin is located within the outer cortex of the soybean nodule. The 3D distribution of (**c**) SAM and **d** *heme* B within the soybean root nodule. Mapping the 3D distribution within soybean nodules of the two metabolic pathways involving SAM during BNF: **e** Polyamine biosynthesis and (**f**) Phosphatidylcholine biosynthesis. For (**f**), we mapped the PC (34:1) as an example because we observed the highest number of phospholipid classes with this fatty acid composition. For both (**e**, **f**), pathway steps known to occur only in bacterium are annotated

or centralized pattern throughout the nodule infection zone (Fig. 2e). Notably though, spermine that is a direct product of aminopropylation transfer via SAM has an asymmetric distribution through the nodule volume, which is a pattern not observed in the 2D images. As such, sectioning was presumably performed in-plane of the uniform concentration of this molecule with respect to the nodule anatomy, which further highlights the importance of molecular tomography for even ostensibly symmetrical systems. To visualize the involvement of SAM in the fate and pathway of PC biosynthesis (Fig. 2f), we used the example of PC (34:1). There are two metabolic routes to the synthesis of PCs in legume nodules [9]: the CDP choline route, a known pathway in plant cells, and the successive methylation route, which is the only known pathway of PC synthesis in rhizobacteria. Our results suggest that PC synthesis through CDP-choline is more prominent in the cortex tissue. Thus, PC from the infection zone seems to arise mainly from bacteroid metabolism through a successive methylation of PE, where SAM serves as a methyl donor. Nonetheless, there is some divergence in SAM and PC localization that might be the result of PC turnover and interconversion into other PLs, and/or a function of the numerous pathways where SAM is utilized as a methyl group donor. Beside PCs, we observed asymmetry in phosphatidylethanolamine (PE) distribution. However, spatial asymmetry is lost as PE (34:1) is converted into phosphatidylserine (PS), and as the lipid head groups are removed from PS, PE, and PC during breakdown to phosphatidic acid (PA). This spatial complexity suggests that the membrane composition of bradyrhizobial species

and surrounding plant cells is well controlled within the soybean nodule system, and that SAM might have a crucial role in this regulation.

In summary, our results demonstrate the utility of high-resolution spatial metabolomics methods, like molecular tomography via MSI, for elucidating the overall complexity of interacting organisms. While molecular tomography has previously been utilized to map metabolic distributions in single-organism systems (e.g., mouse brain [13] or mouse lung [14]), our results demonstrate that this methodology holds particular promise for the study of plant–microbe processes. Especially, where non-imaging modalities can conceal or hint at distributional differences, or when tracking metabolic routes throughout a plant system is desired. Our specific application of this imaging modality to soybean nodules uncovered previously unknown spatial complexity in nodule metabolism, which clearly plays an important role in the ability of these structures to contribute to soybean nitrogen use, and therefore crop productivity and sustainability.

Acknowledgements This material is based on work supported by the U.S. Department of Energy (DOE), Office of Biological and Environmental Research (OBER) under award number DOE-FOA-0001192. This work was performed at EMSL, a national scientific user facility sponsored by the OBER-DOE, located at PNNL, a multidisciplinary national laboratory operated by Battelle for the DOE. Additional support was provided by DOE's Mickey Leland Energy Fellowship (MLEF) Program, University of Missouri's Gus. T. Ridgel Fellowship, and the George Washington Carver Fellowship (BJA). Further support was provided by grant no. 1734145 from the National Science Foundation Plant Genome Program (GS). We thank Yaya Cui for help with growing and inoculating numerous soybean plants.

Compliance with ethical standards

Conflict of interest The authors declare that they have no conflict of interest.

References

1. Guan SH, Gris C, Cruveiller S, Pouzet C, Tasse L, Leru A, et al. Experimental evolution of nodule intracellular infection in legume symbionts. ISME J. 2013;7:1367–77.
2. Ye H, Gemperline E, Venkateshwaran M, Chen R, Delaux PM, Howes-Podoll M, et al. MALDI mass spectrometry-assisted molecular imaging of metabolites during nitrogen fixation in the Medicago truncatula-Sinorhizobium meliloti symbiosis. Plant J. 2013;75:130–45.
3. Gemperline E, Jayaraman D, Maeda J, Ane JM, Li L. Multifaceted investigation of metabolites during nitrogen fixation in Medicago via high resolution MALDI-MS imaging and ESI-MS. J Am Soc Mass Spectrom. 2015;26:149–58.
4. Dupont L, Alloing G, Pierre O, El Msehli S, Hopkins J, Hérouart D, et al. The legume root nodule: from symbiotic nitrogen fixation to senescence. In: Nagata T, editor. Senescence. InTech: Rijeka, Croatia, 2012.
5. Stopka SA, Agtuca BJ, Koppenaal DW, Pasa-Tolic L, Stacey G, Vertes A, et al. Laser ablation electrospray ionization mass spectrometry with ion mobility separation reveals metabolites in the symbiotic interactions of soybean roots and rhizobia. Plant J. 2017;91:340–354.
6. Velickovic D, Anderton CR. Mass spectrometry imaging: towards mapping the elemental and molecular composition of the rhizosphere. Rhizosphere. 2017;3:254–258.
7. Appleby CA. Leghemoglobin and rhizobium respiration. Annu Rev Plant Physiol Plant Mol Biol. 1984;35:443–78.
8. Terakado-Tonooka and Shinsuke F. Involvement of polyamines in the root nodule regulation of soybeans (Glycine max). Plant Root. 2008;2:46–53.
9. Minder AC, de Rudder KEE, Narberhaus F, Fischer HM, Hennecke H, Geiger O. Phosphatidylcholine levels in Bradyrhizobium japonicum membranes are critical for an efficient symbiosis with the soybean host plant. Mol Microbiol. 2001;39:1186–98.
10. Kuzma MM, Winter H, Storer P, Oresnik I, Atkins CA, Layzell DB. The site of oxygen limitation in soybean nodules. Plant Physiol. 1999;119:399–407.
11. Takusagawa F, Kamitori S, Markham GD. Structure and function of S-adenosylmethionine synthetase: crystal structures of S-adenosylmethionine synthetase with ADP, BrADP, and PPi at 2.8 angstrom resolution. Biochemistry. 1996;35:2586–96.
12. Watrous JD, Phelan VV, Hsu CC, Moree WJ, Duggan BM, Alexandrov T, et al. Microbial metabolic exchange in 3D. ISME J. 2013;7:770–80.
13. Eberlin LS, Ifa DR, Wu C, Cooks RG. Three-dimensional vizualization of mouse brain by lipid analysis using ambient ionization mass spectrometry. Angew Chem Int Ed. 2010;49:873–6.
14. Jones EE, Quiason C, Dale S, Shahidi-Latham SK. Feasibility assessment of a MALDI FTICR imaging approach for the 3D reconstruction of a mouse lung. J Am Soc Mass Spectrom. 2017;28:1709–15.

Supplemental material for

Observed metabolic asymmetry within soybean root nodules reflects unexpected complexity in rhizobacteria-legume metabolite exchange

Dušan Veličković[1], Beverly J. Agtuca[2], Sylwia A. Stopka[3], Akos Vertes[3], David W. Koppenaal[1], Ljiljana Paša-Tolić[1], Gary Stacey[2], Christopher R. Anderton[1]

[1] Environmental Molecular Sciences Laboratory, Earth and Biological Sciences Directorate, Pacific Northwest National Laboratory, 902 Battelle Boulevard, Richland, WA USA 99354;

[2] Divisions of Plant Sciences and Biochemistry, C. S. Bond Life Sciences Center, University of Missouri, Columbia, MO USA 65211;

[3] Department of Chemistry, W. M. Keck Institute for Proteomics Technology and Applications, The George Washington University, Washington, DC USA 20052

*Christopher.Anderton@pnnl.gov; 902 Battelle Boulevard, Richland, WA USA 99354; 509-371-7970

Text Summary

Experimental procedures: Plant growth, Sample preparation for MALDI-MSI, MALDI-MSI, and Metabolite identification

Figure S1. Demonstrating the utility of high mass resolution and mass accuracy measurements provided by MALDI-FTICR-MSI for differentiating metabolites in situ.

Figure S2. Distribution of identified small molecules and secondary metabolites through the central section of soybean nodule, as revealed with MALDI-FTICR-MSI.

Figure S3. Distribution of identified phospholipids through the central section of the soybean nodule, as revealed with MALDI-FTICR-MSI.

Figure S4. Optical images of cross-sections of WT and *nif*H- soybean nodules.

Figure S5. Distributions and abundances of metabolites that are measurably different between WT and *nif*H$^-$ mutant soybean nodules.

Table S1. Peak assignments in positive-ion mode profiling MALDI-FTICR mass spectra of soybean root nodules.

Table S2. Peak assignments in negative-ion mode profiling MALDI-FTICR mass spectra of soybean root nodules.

Table S3. MALDI-FTICR-MSI metabolic coverage of some pathways in soybean root nodule based on SoyKB database.

Table S4. The average Pearson's correlation coefficients of SAM, ADP, and *heme* B.

EXPERIMENTAL PROCEDURES

Plant Growth

Rhizobial cells (*Bradyrhizobium japonicum*) USDA110 wild-type (WT) and fix-mutant H1 (*nif*H-) were inoculated into HM medium (Cole and Elkan, 1973) (HEPES, 1.3 g/L; MES, 1.1 g/L; Na_2HPO_4, 0.125 g/L; Na_2SO_4, 0.25 g/L; NH_4Cl, 0.32 g/ L; $MgSO_4 \cdot 7H_2O$, 0.18 g/L; $FeCl_3$, 0.004 g/L; $CaCl_2 \cdot 2H_2O$, 0.013 g/L; yeast extract, 0.25 g/L; D-Ara, 1 g/L; sodium gluconate, 1 g/L; and pH 6.6), supplemented with 25 mg/L of tetracycline and 100 mg/L of spectinomycin for wild-type and 100 mg/L of kanamycin and spectinomycin for *nif*H-. The cells were then incubated and maintained for 2 d at 30 °C in an orbital shaker (MaxQ400, Thermo Scientific, Waltham, MA) set to 180 rpm. Once cellular growth reached 10^8 cells/mL, as measured by optical density (OD600= 0.8), the culture was centrifuged at 800 × g for 10 min, washed three times with DI water, and used for seedling inoculation. Soybean seeds (*Glycine max* Williams 82), sterilized with 20% (v/v) bleach for 10 min and rinsed five times in sterile water, were planted into pots containing a mixture of autoclaved 3/1 vermiculite/perlite, respectively. The plants were grown in a greenhouse at 30 °C with a 16 h light/8 h dark cycle, and at day 3 the seedlings were inoculated with 1 mL of *B. japonicum* suspension per seedling on soil. At day 21 of growth, the roots with attached nodules were freshly harvested, plunged into liquid nitrogen, and stored at -80 °C until further use.

Sample preparation for 2D and 3D MALDI-MSI

Small root sections with attached nodule and individual nodules (without attached root) were excised from frozen soybean roots with a razor blade. These were individually embedded in 2.5 % carboxymethyl cellulose (CMC) and quickly frozen on a bed of dry ice. A carbohydrate rod (spaghetti) was embedded next to individual nodules to serve as positional marker during 3D image reconstruction. Embedded tissue was then mounted and cryosectioned (CryoStar NX70, Thermo Scientific), where the sample chuck and cutting blade were maintained at -13 °C and -16 °C, respectively. 10 µm thick tissue sections were taken orthogonal to length of the root or carbohydrate rod. The sections were thaw-mounted onto indium tin oxide (ITO) glass slides (BrukerDaltonics). For comparing the metabolite distribution pattern between different WT nodules, the central

cross-sections of seven different nodules from different growth batches were mounted on ITO slides, so that sections from only one sample type are present on one ITO slide. For comparison of nifH- and WT strains, two random batches of both nifH- and WT strains were compared by randomly picking one nodule from each batch (four nodules in total). The central cross-sections of each nodule pair (WT and nifH-) were mounted on the same ITO slide and analyzed in the same imaging run. This was repeated for the for the second pair of samples. For 3D MSI, one of every fifth section from the top to bottom of the nodule was mounted, where a total of ~30 sections per ITO slide were mounted. Each section was mounted facing towards the side previously in contact with rest of the tissue, as to avoid positioning error of 180° during stacking of 2D images.

Application of MALDI matrix was performed using HTX TM-Sprayer (HTX Technologies, Chapel Hill, NC, USA) (Gemperline et al., 2015, Anderton et al., 2016). DHB (2, 5-dihydroxybenzoic acid) and norharmane were used for positive and negative ion analysis mode, respectively. For DHB, 40 mg/mL in 50% MeOH was sprayed with 16 passes at 50 µL/min at 80 °C with spray spacing of 3 mm. For norharmane, 7 mg/mL in $CHCl_3$:MeOH (2:1) was used, and seven passes were sprayed at 120 µL/min and 30 °C, with a spray spacing of 2 mm. A spray pressure of 10 psi (N_2), a spray velocity of 1200 mm/min, and a sprayer nozzle distance from the sample of 40 mm was maintained for all samples.

MALDI-MSI

Mass spectrometry imaging was performed on a 15T MALDI-FTICR-MS (Bruker Daltonics) equipped with a SmartBeam II laser source (355 nm, 2 kHz). Data were collected in four different modes: optimized for m/z 92-500 (for low m/z values) and optimized for m/z 400-2000 (for high m/z values) in both positive and negative polarity. External calibration of instrument was performed using TuneMix (Agilent), resulting in mass measurement accuracy typically within 1 ppm across the entire m/z range. The laser was stepped across the sample in 50 µm increments (accumulating 200 laser shots per step), and because images were acquired from every fifth section, our lateral resolution for all measurement was 50 µm in all three dimensions. Image data was acquired using FlexImaging (v 4.1, Bruker Daltonics). Compass DataAnalysis was used

for recalibration of acquired spectra using MALDI matrix peaks as internal calibrants. Deisotoping of mass spectra was performed using mMass 5.5.0 software. Additional image processing (i.e., peak alignment, segmentation, determining co-localized m/z values, and calculation of Pearson correlation coefficients) and visualization of image data were performed using SCiLS Lab (GmbH, Bremen, Germany). 3D MALDI images were created using the additional 3D tool feature in SCiLS Lab. All images were normalized to the total ion current.

Metabolite identification

Metabolites were identified by matching accurate mass (mass accuracy < 1 ppm) with the METLIN database (Supplementary Table 1 and 2), relying both on available literature coverage of legume nodulation metabolites (Brechenmacher et al., 2010, Vauclare et al., 2013, Ye et al., 2013, Gemperline et al., 2015), and LAESI-ion mobility separation-MS and tandem MS analysis of soybean nodules performed by our group previously (Stopka et al., 2017). Additional confirmation of molecular formulas was based on correlating the ion images of the monoisotopic peak with that of the naturally abundant isotopic peaks of the same molecule (Palmer et al., 2017).

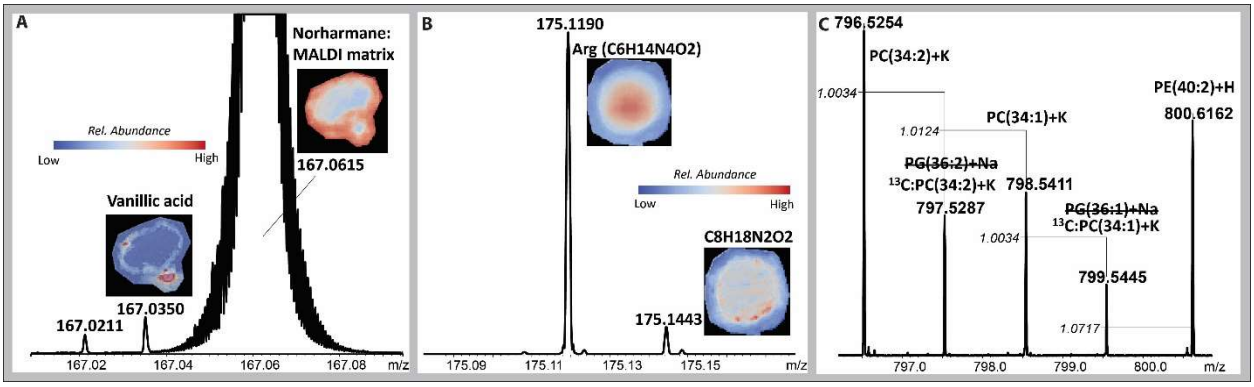

Figure S1. Demonstrating the utility of high mass resolution and mass accuracy measurements provided by MALDI-FTICR-MSI for differentiating metabolites in situ, where (**a**) vallinic acid was resolvable from the matrix peak of norharmane (matrix interference with analytes of interest is common with lower resolving power mass analyzers), (**b**) resolving metabolites with same nominal mass but different spatial distributions is easier, and (**c**) matching detected peaks with naturally occurring isotopes and their relative abundances can provide higher confidence in molecule annotations.

Recent introduction of ultrahigh performance mass spectrometers within imaging workflows has provided a significant advance in MSI, by allowing imaging of small metabolites more attainable with the high mass resolving power and mass accuracy these mass analyzers provide. In our work, the high mass accuracy and resolution of the 15T FTICR-MALDI-MSI enabled us to resolve metabolites with the same nominal masses, and thus to unambiguously identify elemental composition (molecular formula) of any signal of interest. The benefit of ultrahigh resolution and mass accuracy used in our approach (Supplemental Figure 1) is demonstrated through three important imaging issues which impede analysis using lower resolving power instruments (Gemperline et al., 2015). First, we were able to analyze in the low m/z range (Supplemental Figure 1a), where highly abundant MALDI matrix-related signals are resolvable from some endogenous signals. One of the examples is imaging of vanillic acid, m/z 167.0351 [M-H]. With a lower resolution MS analyzer, this signal would be convoluted with the dominant signal of norharmane, which we used as the MALDI matrix in negative ion mode, and thus it would be missed. Second, compounds with the same nominal masses can more readily be resolved. An example is arginine (m/z 175.1190, [M+H]) and an unknown signal about 25 mDa apart (m/z 175.1443), which could be ascribed a molecular formula of $C_8H_{18}N_2O_2$ [M+H]. There is noticeable difference in the localization of these two metabolites, where arginine is present with highest abundance in central part of the

nodule, while the signal at m/z 175.1443 co-localizes with the nodule cortex. Without ultrahigh mass resolution, those two metabolites would be present under one m/z signal and, perhaps, wrongly attributed solely to arginine (Supplemental Figure 1b). Third, ultrahigh mass accuracy enables us to discriminate between isotopic forms and the degree of saturation of phospholipids, Supplemental Figure 1c. An example is an ion at m/z 797.5287, which could be assigned to the sodium adduct of phosphatidylglycerol PG (36:2) (theoretic m/z 797.5303, hence a mass error of 2.01 ppm between measured and theoretical values). However, high accuracy analysis reveals that this ion is actually the ^{13}C isotopic form of phosphatidylcholine PC (34:2) [M+K], which is present as a monoisotopic ion at m/z 796.5254. The mass difference of 1.0034 Da is exactly the same as the difference between ^{13}C and ^{12}C isotope, and the intensity ratio of these two peaks matches well with the simulated isotopic distribution for PC (34:2). A very similar conclusion could be derived for the ion at m/z 799.5445, which could be wrongly interpreted as PG (36:1), as opposed to the naturally abundant $^{13}C_2$- PC (34:2) [M+K] ion. Thus, it is clear that without high performance mass analyzers, imaging and identification of small metabolites and phospholipids would be very ambiguous (Zabrouskov et al., 2001).

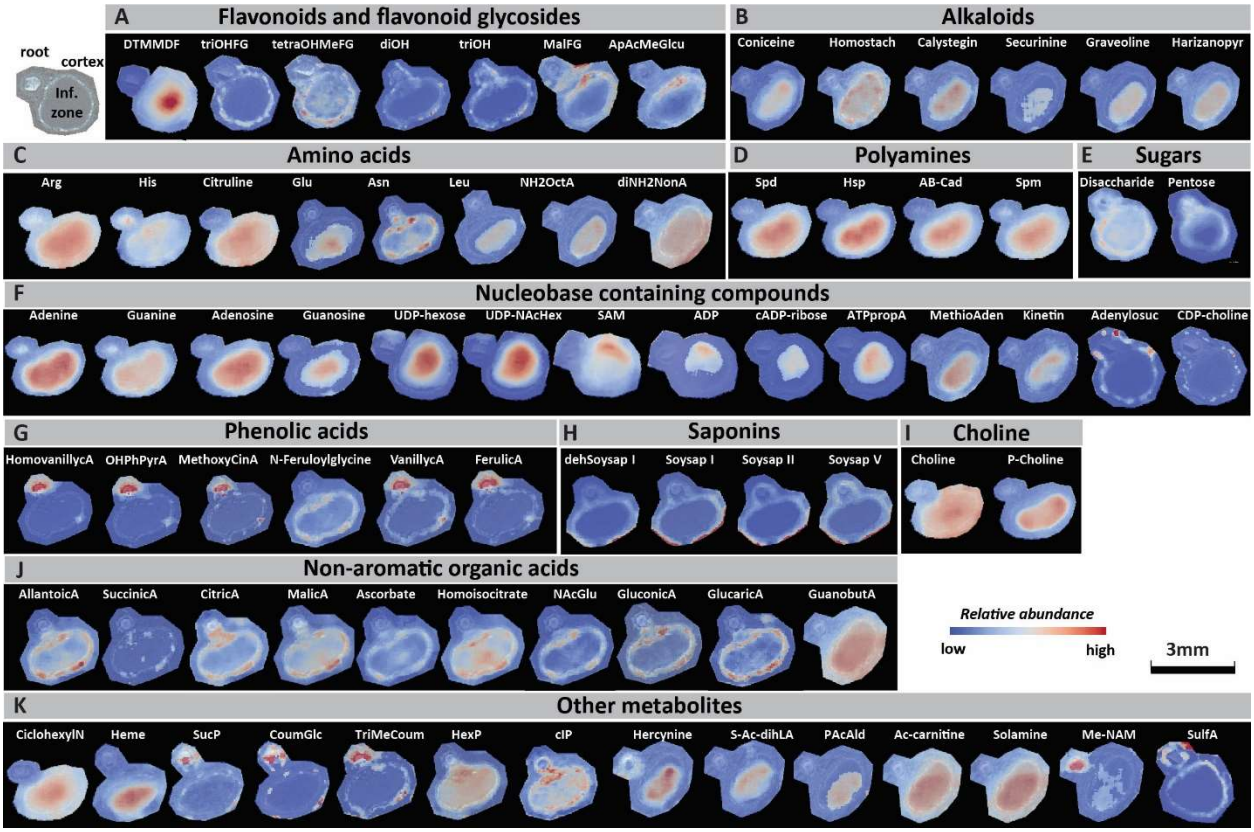

Figure S2. Distribution of identified small molecules and secondary metabolites through the central section of soybean nodules as revealed with MALDI-FTICR-MS imaging. The distribution of (**a**) flavonoids and flavonoid glycosides— *DTMMDF: dihydroxytetramethoxy methylendioxy flavone; triOHFG: trihydroxyflavon glucoside; tetraOHMeFG: tetrahydroxymethoxyflavone glucoside; diOHF: dihydroxyflavone; triOHF: trihydroxyflavone; MalFG: flavon malonyl glucoside; ApAcMeGlcu:Apigenin (acetyl)-methylglucuronide—,* (**b**) Alkaloids, (**c**) Amino acids— *NH2OctA: aminooctanoic acid; diNH2NonA: diaminononanoate*—, (**d**) **b**iological polyamines—*Spd: spermidine; Hsp: homospermidine; AB-Cad: aminobutyl cadaverin; Spm: spermine*—, (**e**) Sugars, (**f**) nucleobase containing compounds— *SAM: S-adenosyl methionine; MethioAden: deoxy-(methylthio) adenosine*—, (**g**) phenolic acids— *OHPhPyrA: hydroxyohenylpyruvic acid—,* (**h**) saponins, (**i**) cholines, (**j**) non-aromatic organic acids— *NAcGlu: N-acetyl- glutamic acid*—, and (**k**) others molecules involved in diverse metabolic pathways in soybean nodule— *CyclohexylN: cyclohexylamine; SucP: sucrose-phosphate; CoumGlc: coumarin glucoside; triMeCoum: trimethoxycoumarines; cIP: inositol cyclic phosphate; S-Ac-dihLA: S-acetyldihydrolipoamide; PAcAldehyde:Phosphonoacetaldehyde; Ac-carnitine: acetycarnitine; Me-NAM: methylnicotineamide; SulfA: sulfuric acid*— are visualized. All images are normalized using the total ion count and color bar is adjusted for each image individually to provide best visualization of ion intensity differences. Lateral resolution is 50 µm. Non-standard abbreviations were explained.

To provide insights into metabolite origin and flow throughout the nodule, we imaged soybean root nodules with the root portion still attached. We found several distinct metabolite distribution patterns that could be visualized across the soybean root and adjoining nodule tissue. Specifically, a large number of metabolites show co-localization within the nodule cortex (e.g., soyasaponins, gluconic acid, CDP-choline, hydroxyphenylpyruvic acid), a few metabolites were more abundant in the root portion

than in the nodule itself (e.g, phenolic acids, trimethoxycoumarin, methylnictonineamide), and some of metabolites show similar abundance in both root vascular and nodule tissues (e.g., histidine, guanine, hexoso-phosphate). Moreover, there are a number of metabolites that were not observed in the root portion. These include several metabolites that are highly concentrated in the center of the nodule (e.g., dihydroxytetramethoxy methylendioxy flavone [DTMDF], UDP-hexose, UDP-N-Acetyl-hexosamine, *heme* B), and are uniformly spread throughout the whole infection zone (e.g., arginine, adenine, choline, guanidinobutyric acid).

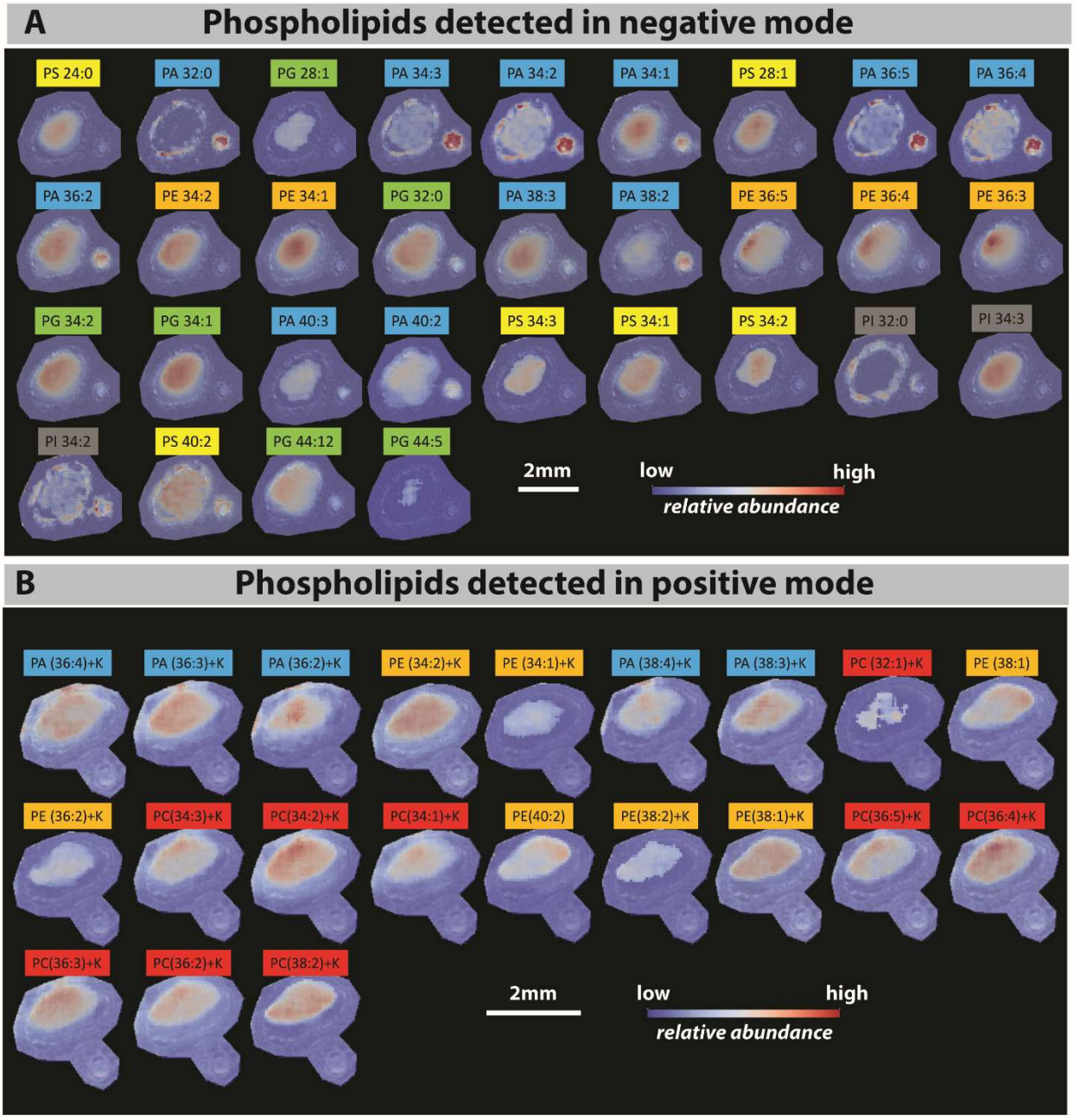

Figure S3. Distribution of identified phospholipids through the central section of the soybean nodule. (**a**) the phospholipids detected in negative mode as $[M\text{-}H]^-$ ions and the (**b**) phospholipids detected in positive mode as $[M+K]^+$ or $[M+H]^+$ ions are shown. All ion images are normalized using the total ion count (TIC) and color bar is adjusted for each ion image individually to provide best visualization of ion intensity differences. Lateral resolution is 50 µm. Each phospholipid class is highlighted with a unique color: yellow: phosphatidylserines (PS); blue: phosphatidic acids (PA); green: phosphatidylglycerols (PG); orange: phosphatidylethanolamines (PE); red: phosphatidylcholines (PC); gray: phosphatidylinositol (PI).

The majority of species detected in both positive and negative mode MALDI-MS (grouped between 700 and 900 *m/z*) originate from phospholipids (PL). These molecules are important constitutes of cell membranes and have been study extensively in plants by MALDI-MSI (Horn et al., 2012, Sturtevant et al., 2017). The high abundance of PL-related signals in soybean nodule system is in accordance with previous estimates suggesting that plant membrane biogenesis needs to be upregulated several fold in order to provide for infection thread development, symbiosme membrane formation, and other membranes involved in nodule development and function (Roth and Stacey, 1989). In positive ion mode we were able to map $[M+H]^+$ and $[M+K]^+$ pseudomolecular ion species of phosphatidic acids (PA), phosphatidylethanolamines (PE), and phosphatidylcholines (PC). All PLs detected in positive ion mode showed co-localization with the infection region, but with different distribution patterns. Using negative ion mode, we additionally determined phophatydilinositols (PI), phosphatydilglycerols (PG), and phosphatydilserines (PS) co-localized either with cortex or in specific compartments of infection zone. Some PLs were detected in both positive and negative ion mode, like PA (36:2), PE (34:2), and PE (34:1). In each case, their localization was consistent between polarities, showing the robustness and verity of the visualization method. Interestingly, we observed that even inside a single class of PLs large distributional differences were measurable. A striking example of this is where PAs were co-localized with the cortex (PA 32:0), uniformly distributed through the entire section (PA 36:4, PA 40:2), asymmetrically distributed within the infection zone (PA 36:4, PA 36:3), or showed centralized distribution pattern (PA 34:1, PA 36:2, PA 38:3, PA 36:2). Such differences in compartmentalization of PL suggests that metabolic pathways for these metabolites occurred heterogeneously within the soybean nodule.

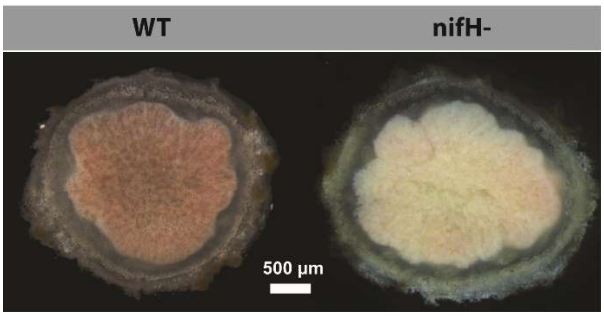

Figure S4. Optical images of cross-sections of WT and *nif*H- soybean nodules showing the differences in color of the infection zone between strains. The reddish color is a result of the presence of legheamoglobin's chromophore (*heme* B).

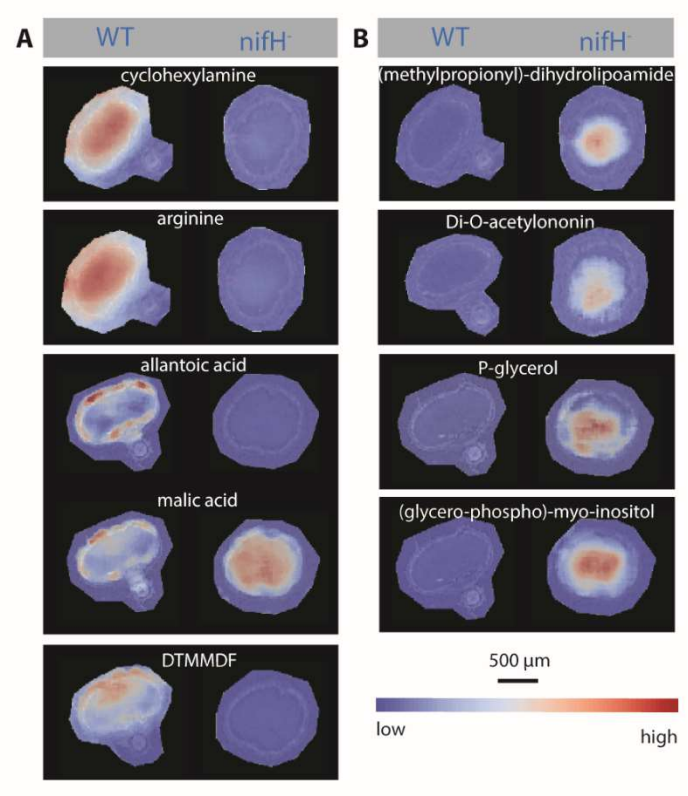

Figure S5. Distributions and abundances of metabolites that are measurably different between WT and nifH$^-$ mutant soybean nodules. The rest of metabolites annotated in Figure S2 show similar distribution patterns and abundances between two strains. (**a**) Metabolites imaged almost exclusively in WT strain. Although not differently distributed between two strains, malic acid is depicted together with allantoic acid to provide general insight into differences in C source input and N source output of symbiotic system, respectively. These results suggest that host doesn't sanction ineffective nodules by limiting their energy supply, given that malic acid was not found as discriminant molecule between WT and nifH- mutant. Therefore, the hypothesis that limitation in oxygen is main host-sanction mechanism (Kiers et al., 2003) is indirectly supported by our study. (**b**) Metabolites imaged almost exclusively in nifH$^-$ mutant. Each WT and nifH$^-$ pair is analyzed in the same experiment with the same image adjustment processing.

Table S1. Peak assignments in positive-ion mode profiling MALDI-FTICR mass spectra of soybean root nodules. Metabolites are detected as $[M+H]^+$ species unless otherwise is specified. Levels of confidence: Level 1: identified compounds based on ultra-high mass accuracy (<1 ppm) and at least one more independent orthogonal data (tandem MS or collision cross section (ccs)); Level 2a: Putatively annotated compounds based upon ultra-high mass accuracy (<1 ppm) and soybean/legume nodule literature coverage; Level 2b: Putatively annotated compounds according solely to ultra-high mass accuracy (<1 ppm) as was originally defined by the Metabolomics Standard Initiative.(Sumner et al., 2007)

Metabolite	Measured m/z	Theoretical m/z	Error (ppm)	MSI level	Localization
Cyclohexylamine [a]	100.1121	100.1121	0.00	1	Infection r
Choline [a,b]	104.1070	104.1070	0.00	1	Infection r
Coniceine	126.1278	126.1277	0.79	2b	Infection r
Leucine [b]	132.1020	132.1019	0.76	2a	Infection r
Asparagine [c]	133.0608	133.0608	0.00	2a	Cortex
Adenine [a]	136.0619	136.0620	0.73	1	Infection r
Methylnicotineamide	137.0710	137.0709	0.73	2b	Infection r
Guanidinobutanoic acid	146.0925	146.0924	0.68	2b	Infection r
Spermidine [a]	146.1653	146.1652	0.68	1	Infection r
Guanine [a]	152.0568	152.0567	0.66	1	Infection r
Histidine [b]	156.0768	156.0768	0.00	2a	Infection r
Homostachydrine/Lentiginosine	158.1176	158.1176	0.00	2b	Infection r
Guanidinovaleric acid	160.1081	160.1081	0.00	2b	Infection r
Homospermidine [d]	160.1809	160.1808	0.62	2a	Infection r
Phosphonoacetaldehyde+K	162.9558	162.9557	0.61	2b	Infection r
Aminobutyl cadaverin (aminobutyl-cad)	174.1966	174.1965	0.57	2b	Infection r
Arginine [a,b,c]	175.1190	175.1190	0.00	1	Infection r
Calystegin	176.0918	176.0917	0.57	2b	Infection r
Citruline [a]	176.1031	176.1030	0.57	1	Infection r
Phosphocholine [a]	184.0734	184.0733	0.54	1	Infection r
Diaminononanoate+K	189.1599	189.1598	0.53	2b	Infection r
Aminooctanoic acid+K	198.0891	198.0891	0.00	2b	Infection r
Spermine	203.2231	203.2230	0.49	2b	Infection r
Acetylcarnitine	204.1231	204.1230	0.49	2b	Infection r
Kinetin	216.0881	216.0880	0.46	2b	Infection r
Solamine	216.2435	216.2434	0.46	2b	Infection r
Acetyldihydrolipoamide +H-H2O	232.0830	232.0830	0.00	2b	Infection r
Securinine+Na	240.0995	240.0995	0.00	2b	Infection r
Adenosine [a]	268.1042	268.1040	0.75	1	Infection r
Deoxy(methylthio)adenosine	298.0970	298.0968	0.67	2b	Infection r
Graveoline/avenalumin II +Na	302.0787	302.0788	0.33	2b	Infection r
Harzianopyridone+K	320.0893	320.0895	0.62	2b	Infection r
Guanosine+K	322.0547	322.0548	0.31	2b	Infection r
coumarin glucosides	363.0689	363.0687	0.55	2b	Cortex
Disaccharide +K [a,b]	381.0793	381.0794	0.26	1	Cortex Inner

S-adenosyl methionine [a,c]	399.1444	399.1445	0.25	1	Infection r
Sucrose-phosphate	423.0900	423.0898	0.47	2b	Cortex Outer
ADP [a]	428.0366	428.0367	0.23	1	Infection r
Trihydroxyflavon glucoside + Na [a]	471.0899	471.0898	0.21	1	Cortex Inner
Adenylosuccinate+K	502.0376	502.0372	0.80	2b	Cortex Inner
Tetrahydroxymethoxyflavone glucoside + K	517.0954	517.0953	0.19	2b	Cortex Inner
CDP-choline +K	527.0709	527.0705	0.76	2b	Cortex Inner
Apigenin(acetyl-methylglucuronide)+K	541.0743	541.0743	0.00	2b	Cortex
cADP-ribose [a]	542.0683	542.0684	0.18	1	Infection r
ATP-propionic acid [c]	580.0241	580.0242	0.17	2a	Infection r
Heme *B* [a,b,c]	616.1766	616.1768	0.32	1	Infection r
PA (36:4)+K	735.4362	735.4362	0.00	2b	Infection r
PA (36:3)+K	737.4520	737.4518	0.27	2b	Infection r
PA (36:2)+K	739.4675	739.4675	0.00	2b	Infection r
PE (34:2)+K	754.4783	754.4784	0.13	2b	Infection r
PE (34:1)+K	756.4942	756.4940	0.26	2b	Infection r
PC(34:3)	756.5538	756.5538	0.00	2b	Infection r
PC (34:2) /MMPE(36:2)	758.5695	758.5694	0.13	2b	Infection r
PC (34:1)	760.5853	760.5851	0.26	2b	Infection r
PA (38:4)+K	763.4676	763.4675	0.13	2b	Infection r
PA (38:3)+K	765.4831	765.4831	0.00	2b	Infection r
PC (32:1)+K/MMPE(34:1)+K	770.5097	770.5097	0.00	2b	Infection r
PE (38:1)	774.6007	774.6007	0.00	2b	Infection r
PE (36:2)+K	782.5099	782.5097	0.26	2b	Infection r
PC(36:3)	784.5852	784.5851	0.13	2b	Infection r
PC(36:2)	786.6008	786.6007	0.13	2b	Infection r
PC (34:2)+K/MMPE(36:2)+K	796.5254	796.5253	0.13	2b	Infection r
PC(34:1)+K	798.5411	798.5410	0.13	2b	Infection r
PE(40:2)	800.6162	800.6164	0.25	2b	Infection r
PE(38:2)+K	810.5410	810.5409	0.12	2b	Infection r
PE (38:1)+K	812.5564	812.5566	0.25	2b	Infection r
PC (38:2)	814.6317	814.6320	0.37	2b	Infection r
PC (36:5) +K	818.5093	818.5097	0.49	2b	Infection r
PC (36:4)+K	820.5253	820.5253	0.00	2b	Infection r
PC (36:3) + K	822.5409	822.5410	0.12	2b	Infection r
PC (36:2)+K	824.5564	824.5566	0.24	2b	Infection r
PE(40:2)+K	838.5719	838.5721	0.24	2b	Infection r
PC(38:2)+K	852.5875	852.5879	0.47	2b	Infection r
Soyasaponin II +K [a]	951.4717	951.4714	0.32	1	Cortex Outer
Dehydrosoyasaponin I +K [a]	979.4666	979.4663	0.31	1	Cortex Outer
Soyasaponin I +K [a]	981.4822	981.4820	0.20	1	Cortex Outer

[a] Chemical species assigned based on in-house LAESI MSMS and/or ion mobility results.(Stopka et al., 2017)
[b] Chemical species assigned based on (Ye et al., 2013)
[c] Chemical species assigned based on (Gemperline et al., 2015)
[d] Chemical species assigned based on (Vauclare et al., 2013)
[e] Chemical species assigned based on (Brechenmacher et al., 2010).

Table S2. Peak assignments in negative-ion mode profiling MALDI FTICR mass spectra of soybean root nodules. Metabolites are detected as $[M-H]^-$ species. Levels of confidence: Level 1: identified compounds based on ultra-high mass accuracy (<1ppm) and at least one more independent orthogonal data (tandem MS or collision cross section (ccs)); Level 2a: Putatively annotated compounds based upon ultra-high mass accuracy (<1ppm) and soybean/legume nodule literature coverage; Level 2b: Putatively annotated compounds according solely to ultra-high mass accuracy (<1ppm) as was originally defined by the Metabolomics Standard Initiative.(Sumner et al., 2007)

Metabolite	Measured m/z	Theoretical m/z	Error (ppm)	MSI level	Localization
Sulfuric acid	96.9601	96.9601	0.00	2b	Cortex
Succinic acid [b]	117.0193	117.0193	0.00	2a	Cortex
Asparagine [c]	131.0462	131.0462	0.00	2a	Cortex
Malic acid [a,b]	133.0143	133.0142	0.75	1	Infection r
Glutamate [a c d e]	146.0458	146.0459	0.68	1	Infection r
Pentose [a,b]	149.0456	149.0455	0.67	1	Cortex
Vanillic acid [a]	167.0350	167.0350	0.00	1	Cortex
Ascorbic acid [b]	175.0248	175.0248	0.00	2a	Infection r
Allantoic acid [e]	175.0473	175.0473	0.00	2a	Cortex
Methoxycinnamic acid	177.0558	177.0557	0.56	2b	Cortex
Hydroxyohenylpyruvic acid	179.0351	179.0350	0.56	2b	Cortex
Homovanillic acid	181.0507	181.0506	0.55	2b	Cortex
Acetyl-Glutamic acid	188.0565	188.0564	0.53	2b	Cortex
Citric acid	191.0197	191.0197	0.00	2b	Cortex
Ferulic acid [e]	193.0507	193.0506	0.52	2a	Cortex
Gluconic acid [a]	195.0511	195.0510	0.51	1	Cortex
Me-citrate/homoisocitrate	205.0354	205.0354	0.00	2b	Infection r
Glucarate	209.0303	209.0303	0.00	2b	Cortex
Trimethoxycoumarines	235.0613	235.0612	0.43	2b	Cortex
Inositol cyclic phosphate	241.0119	241.0119	0.00	2b	Cortex
N-Feruloylglycine	250.0721	250.0721	0.00	2b	Cortex
Dihydroxyflavone [a]	253.0507	253.0506	0.40	1	Cortex
Hex-phosphate [a,b]	259.0224	259.0224	0.00	1	Infection r
Trihydroxyflavone [a]	269.0457	269.0455	0.74	1	Cortex
Dihydroxytetramethoxy methylendioxy flavone (DTMMDF) [a]	417.0828	417.0827	0.24	1	Infection r
flavon malonyl glucoside [a]	485.1089	485.1089	0.00	1	Cortex Outer
UDP-hexose [a,b]	565.0477	565.0477	0.00	1	Infection r
Flavonoid diglycoside	595.1305	595.1305	0.00	2b	Cortex Inner
UDP-NAcGlcN [a]	606.0742	606.0743	0.16	1	Infection r
PS (24:0)	622.3726	622.3725	0.16	2b	Cortex Inner
PA (32:0)	647.4656	647.4657	0.15	2b	Cortex Inner
PG (28:1)	663.4242	663.4243	0.15	2b	Infection r
PA (34:3)	669.4500	669.4501	0.15	2b	Cortex Inner
PA (34:2)	671.4656	671.4657	0.15	2b	Cortex Inner

PA (34:1)	673.4813	673.4814	0.15	2b	Infection r
PS(28:1)	676.4195	676.4195	0.00	2b	Infection r
PA (36:5)	693.4498	693.4501	0.43	2b	Cortex Inner
PA (36:4)[a]	695.4657	695.4657	0.00	1	Cortex Inner
PA(36:2)	699.4969	699.4970	0.14	2b	Infection r
PE (34:2)[a]	714.5078	714.5080	0.28	1	Infection r
PE (34:1)[a]	716.5234	716.5236	0.28	1	Infection r
PG(32:0)	721.5024	721.5025	0.14	2b	Infection r
PA(38:3)	725.5126	725.5127	0.14	2b	Infection r
PA(38:2)	727.5282	727.5283	0.14	2b	Infection r
PE(36:5)	736.4922	736.4923	0.14	2b	Infection r
PE(36:4)	738.5079	738.5079	0.00	2b	Infection r
PE(36:3)	740.5235	740.5236	0.14	2b	Infection r
PG(34:2)	745.5024	745.5025	0.13	2b	Infection r
PG (34:1)[a]	747.5181	747.5182	0.13	1	Infection r
PA(40:3)	753.5439	753.5440	0.13	2b	Infection r
PA(40:2)	755.5595	755.5596	0.13	2b	Infection r
PS(34:3)	756.4819	756.4821	0.26	2b	Infection r
PS(34:2)	758.4975	758.4978	0.40	2b	Infection r
PS (34:1)	760.5131	760.5134	0.39	2b	Infection r
PI(30:4)	773.4241	773.4247	0.78	2b	Cortex Inner
PG (36:2)[a]	773.5336	773.5338	0.26	1	Infection r
PI(32:0)	809.5185	809.5186	0.12	2b	Cortex Inner
PI(34:3)	831.5027	831.5029	0.24	2b	Cortex Inner
PI(34:2)	833.5185	833.5186	0.12	2b	Cortex Inner
PS(40:2)	842.5914	842.5917	0.36	2b	Infection r
Soyasaponin II [a]	911.5015	911.5010	0.55	1	Cortex Outer
Dehydrosoyasaponin I [a]	939.4960	939.4958	0.21	1	Cortex Outer
Soyasaponin I [a]	941.5124	941.5115	0.96	1	Cortex Outer

[a] Chemical species assigned based on in-house LAESI MSMS and/or ion mobility results.(Stopka et al., 2017)
[b] Chemical species assigned based on (Ye et al., 2013)
[c] Chemical species assigned based on (Gemperline et al., 2015)
[d] Chemical species assigned based on (Vauclare et al., 2013)
[e] Chemical species assigned based on (Brechenmacher et al., 2010)

Table S3. MALDI-FTICR-MSI metabolic coverage of some pathways in soybean root nodule based on SoyKB database.

Pathway	Kegg	Compound	% coverage
Purine metabolism	cpd:C00008	ADP	13.1
	cpd:C00212	Adenosine	
	cpd:C00147	Adenine	
	cpd:C03794	Adenylosuccinate	
	cpd:C00499	Allantoic acid	
	cpd:C00059	Sulfuric acid	
	cpd:C00242	Guanine	
	cpd:C00387	Guanosine	
Glyoxylate and dicarboxylate metabolism	cpd:C00158	Citric acid	17.7
	cpd:C00149	Malic acid	
	cpd:C00042	Succinic acid	
Zeatin biosynthesis	cpd:C00008	ADP	15.8
	cpd:C00147	Adenine	
	cpd:C00029	Uridine diphosphate glucose	
Citrate cycle (TCA cycle)	cpd:C00149	Malic acid	20
	cpd:C00042	Succinic acid	
	cpd:C00158	Citric acid	
	cpd:C16255	S-Acetyldihydrolipoamide	
Arginine and proline metabolism	cpd:C00327	Citrulline	10.5
	cpd:C00062	L-Arginine	
	cpd:C00025	Glutamate	
	cpd:C00624	N-Acetyl-L-glutamic acid	
	cpd:C00315	Spermidine	
	cpd:C00750	Spermine	
beta-Alanine metabolism	cpd:C00315	Spermidine	16.6
	cpd:C00750	Spermine	
Glutathione metabolism	cpd:C00025	Glutamate	12.3
	cpd:C00315	Spermidine	
	cpd:C00072	Ascorbic acid	
	cpd:C00750	Spermine	
Aminoacyl-tRNA biosynthesis	cpd:C00025	Glutamate	7.5

	cpd:C00062	L-Arginine	
	cpd:C00152	L-Asparagine	
	cpd:C00135	L-Histidine	
	cpd:C00123	L-Leucine	
Aminoacyl-tRNA biosynthesis	cpd:C00818	D-Glucarate	20
	cpd:C00072	Ascorbic acid	
	cpd:C0029	Uridine diphosphate glucose	
Histidine metabolism	cpd:C05575	Hercynine	18.8
	cpd:C00025	Glutamate	
	cpd:C00025	Hercynine	
Glycerophospholipid metabolism	cpd:C00307	CDP-choline	12
	cpd:C00588	Phosphocholine	
	cpd:C00114	Choline	
Alanine, aspartate and glutamate metabolism	cpd:C00042	Succinic acid	22.7
	cpd:C03794	Adenylosuccinate	
	cpd:C00025	Glutamate	
	cpd:C00158	Citric acid	
	cpd:C00152	L-Asparagine	
Tyrosine metabolism	cpd:C00042	Succinic acid	16.7
	cpd:C05582	Homovanillic acid	
	cpd:C01179	4-Hydroxyphenylpyruvic acid	
Nitrogen metabolism	cpd:C00025	Glutamate	6.7
Starch and sucrose metabolism	cpd:C16688	Sucrose-6-phosphate	10
	cpd:C00089	Sucrose	
	cpd:C00029	Uridine diphosphate glucose	

Table S4. The average Pearson's correlation coefficients of SAM, ADP, and *heme* B. Pearson's correlation coefficients were calculated using the SCILS software.

	SAM	**ADP**	***heme* B**
SAM	-	0.80 ± 0.09	0.62 ± 0.09
ADP	0.80 ± 0.09	-	0.62 ± 0.12
***heme* B**	0.62 ± 0.09	0.62 ± 0.12	-
Nodule shape	0.58 ± 0.12	0.59 ± 0.09	0.66 ± 0.13

References

Anderton, C. R., Chu, R. K., Tolic, N., Creissen, A. and Pasa-Tolic, L. (2016). Utilizing a Robotic Sprayer for High Lateral and Mass Resolution MALDI FT-ICR MSI of Microbial Cultures. Journal of the American Society for Mass Spectrometry **27**: 556-559.

Brechenmacher, L., Lei, Z. T., Libault, M., Findley, S., Sugawara, M., Sadowsky, M. J., Sumner, L. W. and Stacey, G. (2010). Soybean Metabolites Regulated in Root Hairs in Response to the Symbiotic Bacterium Bradyrhizobium japonicum. Plant Physiology **153**: 1808-1822.

Cole, M. A. and Elkan, G. H. (1973). Transmissible Resistance to Penicillin-G, Neomycin, and Chloramphenicol in Rhizobium-Japonicum. Antimicrobial Agents and Chemotherapy **4**: 248-253.

Gemperline, E., Jayaraman, D., Maeda, J., Ane, J. M. and Li, L. (2015). Multifaceted investigation of metabolites during nitrogen fixation in Medicago via high resolution MALDI-MS imaging and ESI-MS. J Am Soc Mass Spectrom **26**: 149-158.

Horn, P. J., Korte, A. R., Neogi, P. B., Love, E., Fuchs, J., Strupat, K., Borisjuk, L., Shulaev, V., Lee, Y. J. and Chapman, K. D. (2012). Spatial Mapping of Lipids at Cellular Resolution in Embryos of Cotton. Plant Cell **24**: 622-636.

Kiers, E. T., Rousseau, R. A., West, S. A. and Denison, R. F. (2003). Host sanctions and the legume-rhizobium mutualism. Nature **425**: 78-81.

Palmer, A., Phapale, P., Chernyavsky, I., Lavigne, R., Fay, D., Tarasov, A., Kovalev, V., Fuchser, J., Nikolenko, S., Pineau, C., Becker, M. and Alexandrov, T. (2017). FDR-controlled metabolite annotation for high-resolution imaging mass spectrometry. Nature Methods **14**: 57-60.

Roth, L. E. and Stacey, G. (1989). Bacterium Release into Host-Cells of Nitrogen-Fixing Soybean Nodules - the Symbiosome Membrane Comes from 3 Sources. European Journal of Cell Biology **49**: 13-23.

Stopka, S. A., Agtuca, B. J., Koppenaal, D. W., Pasa-Tolic, L., Stacey, G., Vertes, A. and Anderton, C. R. (2017). Laser Ablation Electrospray Ionization Mass Spectrometry with Ion Mobility Separation Reveals Metabolites in the Symbiotic Interactions of Soybean Roots and Rhizobia. Plant J.

Sturtevant, D., Duenas, M. E., Lee, Y. J. and Chapman, K. D. (2017). Three-dimensional visualization of membrane phospholipid distributions in Arabidopsis thaliana seeds: A spatial perspective of molecular heterogeneity. Biochimica Et Biophysica Acta-Molecular and Cell Biology of Lipids **1862**: 268-281.

Sumner, L. W., Amberg, A., Barrett, D., Beale, M. H., Beger, R., Daykin, C. A., Fan, T. W. M., Fiehn, O., Goodacre, R., Griffin, J. L., Hankemeier, T., Hardy, N., Harnly, J., Higashi, R., Kopka, J., Lane, A. N., Lindon, J. C., Marriott, P., Nicholls, A. W., Reily, M. D., Thaden, J. J. and Viant, M. R. (2007). Proposed minimum reporting standards for chemical analysis. Metabolomics **3**: 211-221.

Vauclare, P., Bligny, R., Gout, E. and Widmer, F. (2013). An overview of the metabolic differences between Bradyrhizobium japonicum 110 bacteria and differentiated bacteroids from soybean (Glycine max) root nodules: an in vitro 13C-and 31P-nuclear magnetic resonance spectroscopy study. Fems Microbiology Letters **343**: 49-56.

Ye, H., Gemperline, E., Venkateshwaran, M., Chen, R., Delaux, P. M., Howes-Podoll, M., Ane, J. M. and Li, L. (2013). MALDI mass spectrometry-assisted molecular imaging of metabolites during nitrogen fixation in the Medicago truncatula-Sinorhizobium meliloti symbiosis. Plant J **75**: 130-145.

Zabrouskov, V., Al-Saad, K. A., Siems, W. F., Hill, H. H., Jr. and Knowles, N. R. (2001). Analysis of plant phosphatidylcholines by matrix-assisted laser desorption/ionization time-of-flight mass spectrometry. Rapid Commun Mass Spectrom **15**: 935-940.